

Tuaimenal A, a meroterpene from the previously  
unexplored deep-sea Irish soft coral of the Genus  
*Drifa*, displays *in silico* binding of the main protease  
of SARS-CoV-2

*Avalon, Nicole E.;<sup>†</sup> Nafie, Jordan;<sup>‡</sup> Dietrick, Sarah G.<sup>†</sup> Young, Ryan M.;<sup>§^</sup> Warrensford, Luke;<sup>†</sup>  
Pittman, Amanda;<sup>†</sup> Kearns, Fiona;<sup>†</sup> Johnson, Mark P.;<sup>§</sup> Woodcock, H. Lee;<sup>†</sup> Allcock, A.  
Louise;<sup>§</sup> Baker, Bill J.<sup>†</sup>*

<sup>†</sup> Department of Chemistry, University of South Florida, Tampa, FL, USA.

<sup>‡</sup> BioTools, Inc., Jupiter, FL, USA.

<sup>§</sup> Department of Zoology, National University of Ireland Galway, Galway, Ireland.

<sup>^</sup>School of Chemistry, National University of Ireland Galway, Galway, Ireland.

**KEYWORDS**

Terpene, Deep Sea, Natural Product, Cnidarian, SARS-CoV-2

## ABSTRACT

Cold water benthic environments are a prolific source of structurally diverse molecules with a range of bioactivity against human disease. Specimens of a previously chemically unexplored soft coral, *Drifa* sp., were collected during a deep-sea cruise that sampled marine invertebrates along the Irish continental margin in 2018. Tuaimenal A (**1**), a compound representing new carbon scaffold with a highly substituted chromene core, was discovered through the exploration of the secondary metabolome of the soft coral through NMR-guided fractionation. VCD analysis was used to determine absolute stereochemistry. This molecule demonstrates a strong profile for inhibition of the main protease of SARS-CoV-2 based on *in silico* docking experiments.

Ninety-five percent of the ocean floor exceeds depths of 1,000 meters where water temperatures are approximately 4 °C.<sup>1</sup> Over half of the 5,100 known coral species are found in the deep sea, where cold water corals create coral gardens in benthic regions ranging from 200 – 1000 m in depth.<sup>1</sup> Utilizing both physiological and biochemical adaptations, cold water corals have adapted to survive in an environment with minimal-to-no light, and with extremely high pressures.<sup>2</sup> One biochemical adaptation is the production of secondary metabolites. These compounds not only confer a competitive advantage to the organisms but also have high rates of affinity to biological targets implicated in human disease.<sup>2</sup> Natural products from the deep sea comprise less than 2% of known natural products; however, the rate of bioactivity from deep-sea compounds is estimated to be as high as 75%.<sup>3</sup>

Across the world's oceans, the phylum Cnidaria is second only to Porifera in the number of new natural products reported annually from invertebrates.<sup>4</sup> Comprising over three thousand species, Octocorallia are a particularly rich source of natural product exploration; roughly eighty percent of bioactive compounds from corals have been isolated from this subclass.<sup>5,6</sup> The Nephtheidae family comprises twenty genera and about five hundred species, including the genus *Drifa*. Known colloquially as cauliflower corals due to their appearance, *Drifa* species thrive in cold water benthic environments (**Fig. 1**). Corals from the family Nephtheidae are known to produce steroidal and other terpenoid secondary metabolites,<sup>5,7</sup> but the chemistry of *Drifa* has yet to be described.



**Figure 1.** Four specimens of *Drifa* sp. (Cnidaria: Anthozoa: Octocorallia: Alcyonacea: Alcyoniina: Nephtheidae) collected at a depth of 823 m from a submarine canyon north of Porcupine Bank on the Irish Continental Margin by *ROV Holland I*, deployed from *RV Celtic Explorer*. For scaling a laser light is used (red dots indicate a span of 10 cm). Subsea photographs are copyright Marine Institute, Oranmore, Ireland. Used with permission.

The emergence of the severe acute respiratory syndrome coronavirus 2 (SARS-CoV-2 virus) from Wuhan, China in late 2019, led to the rapid spread of the highly infectious and pathogenic virus and subsequent declaration of the COVID-19 pandemic by the Center for Disease Control (CDC) in March of 2020.<sup>8-10</sup> The ongoing pandemic caused by the highly-contagious virus in the *Coronaviridae* family is responsible for the deaths of over 2.8 million people worldwide to-date.<sup>11</sup> While vaccinations against SARS-CoV-2 are being administered worldwide, treatment of the disease is limited. Therefore, drug discovery and drug repurposing efforts are underway to find effective treatments for COVID-19 infections.<sup>10,12</sup> SARS-CoV-2 is an enveloped positive-sense single-stranded RNA virus, and its rapid spread depends on both viral and host proteins.<sup>9,13</sup> Four protein targets were selected for *in silico* experiments based on their critical roles in this process. The main protease (Mpro) is viral protease responsible for cleaving twelve non-structural proteins (Nsp4-Nsp16), allowing for the viral maturation of the

pathogen.<sup>9</sup> Inhibition of this protease has been shown to prevent viral replication, making it a suitable drug target.<sup>14,15</sup> Transmembrane Serine Protease 2 (TMPRSS2) assists in the activation and proliferation roles for SARS-CoV-2, and inhibition of this protein can block cell entry.<sup>16</sup> The papain-like protein (PLpro) assists with viral replication by processing non-structural proteins Nsp1-Nsp3.<sup>9</sup> RNA-dependent RNA-polymerase (RdRp) is a critical component for both replication and transcription of this positive-strand RNA virus, and therefore, another important protein to target.<sup>17</sup> Herein we report in silico docking studies of the major SARS-CoV-2 protein targets against a metabolite from *Drifa* sp.

## RESULTS AND DISCUSSION

**Structure Analysis of Tuaimenal A (1).** Tuaimenal A (1)<sup>18</sup> was obtained as a yellow oil with a molecular formula of C<sub>23</sub>H<sub>30</sub>O<sub>4</sub> based on high resolution electrospray ionization mass spectrometry (HRESIMS) ([M + H]<sup>+</sup> of 371.2216 amu; calculated for C<sub>23</sub>H<sub>31</sub>O<sub>4</sub> 371.2217, Δmmu 0.1) and corroborated by NMR data (**Table 1**). The downfield region of the <sup>1</sup>H NMR spectrum (**Fig. S1**), informed by the phase-sensitive gHSQCAD spectrum (**Fig. S3**), revealed several functional groups. The signal at δ<sub>H</sub> 12.31 (OH<sub>a</sub>) (**Fig. 2**) displayed no HSQC correlation to a carbon, suggesting it was on a heteroatom, and its shift was characteristic of an H-bonded phenol. The shift at δ<sub>H</sub> 10.08 (H-11), correlated in the HSQC with δ<sub>C</sub> 191.1 (C-11), both of which are consistent with an aldehyde function. A series of olefinic proton shifts from δ<sub>H</sub> 5.07 to 6.86, taken with twelve olefinic <sup>13</sup>C chemical shifts identified a highly oxidized skeleton; the most deshielded, δ<sub>C</sub> 158.2 (C-6) and 151.4 (C-8) are indicative of olefinic/aromatic oxygen-bearing carbons.

**Table 1.** NMR Spectroscopic Data (400 MHz, CDCl<sub>3</sub>) for tuaimenal A (**1**)

<i>pos</i>	$\delta_C$ , <i>type</i>	$\delta_H$ , <i>mult</i> , <i>J</i> (Hz)	<i>HMBC</i>
2	79.1, C		
3	132.4, CH	5.80, d (10.1)	C-2, C-10, C-12', C-1'
4	116.4, CH	6.86, d (10.1)	C-2, C-9, C-10
5	107.5, C		
6	158.2, C		
7	111.7, C		
8	151.4, C		
9	132.3, C		
10	118.7, C		
11	191.1, CH	10.08, s	C-5, C-6, C-7
12	7.6, CH <sub>3</sub>	2.14, s	C-6, C-7, C-8
1'	40.2, CH <sub>2</sub>	1.78, 2.12, m	
2'	22.6, CH <sub>2</sub>	1.76, 2.13, m	
3'	123.3, CH	5.11, t	C-2', C-5', C-11'
4'	135.8, C		
5'	39.6, CH <sub>2</sub>	1.99, t	
6'	26.6, CH <sub>2</sub>	2.05, m	C-4', C-5', C-7', C-8'
7'	124.1, CH	5.07, t	C-10'
8'	131.4, C		
9'	25.7, CH <sub>3</sub>	1.68, s	C-7', C-8', C-10'
10'	17.7, CH <sub>3</sub>	1.59, s	C-7', C-8', C-9'
11'	16.0, CH <sub>3</sub>	1.58, s	C-5', C-3', C-4'
12'	25.4, CH <sub>3</sub>	1.43, s	C-2, C-3, C-1'
OH <sub>a</sub>		12.31, s	C-5, C-6, C-7, C-8
OH <sub>b</sub>		6.37, s	C-6, C-7, C-8, C-9

Further analysis of the 2D spectra facilitated the development of additional partial structures. The HSQC was used to assign the remainder of the protons to their respective carbons (**Table 1**). Taken with the COSY spectrum (**Fig. S4**), spin-coupled systems could be developed. Vinylic proton  $\delta_H$  6.86 (H-4) shared a COSY correlation and *J* with vinylic proton  $\delta_H$  5.80 (H-3). The singlet vinyl proton  $\delta_H$  5.11 (H-3') shared a COSY correlation with the 3H singlet at  $\delta_H$  1.58 (H<sub>3</sub>-11'). Additionally,  $\delta_H$  1.68 (H<sub>3</sub>-9') showed correlation in the COSY spectrum to  $\delta_H$  5.07 (H-

7') and 1.59 (H<sub>3</sub>-10'), resulting in a vinyl gem-dimethyl group terminating a trisubstituted olefin (Fig. 2).

HMBC data was used to extend the partial structures (Fig. S5). The signal at  $\delta_{\text{H}}$  10.08 (H-11) had multiple correlations, including  $\delta_{\text{C}}$  107.5 (C-5), 158.2 (C-6), and 111.7 (C-7), while  $\delta_{\text{H}}$  2.14 (H<sub>3</sub>-12) shared correlations with C-6, C-7, and  $\delta_{\text{C}}$  151.4 (C-8), forming a conjugated system consisting of two olefins and the aldehyde carbonyl (Fig. 2). A proton at  $\delta_{\text{H}}$  5.80 (H-3) displayed HMBC correlations to  $\delta_{\text{C}}$  79.1 (C-2), 118.7 (C-10), 25.4 (C-12'), and 40.2 (C-1'). Similarly, H-4 displayed HMBC correlation to C-2,  $\delta_{\text{C}}$  107.5 (C-5), and 132.3 (C-9). Olefinic C-9 and C-10 therefore are in conjugation with  $\delta_{\text{C}}$  116.4 (C-4) and 132.4 (C-3). A singlet proton at  $\delta_{\text{H}}$  6.37 (OH<sub>b</sub>) had HMBC correlation to C-8 and C-9 which, taken with the HMBC correlation between H-4 and C-5, establishes an aromatic ring. The C-2 shift is consistent with carbon bearing oxygen; this quaternary carbon had correlations from H-3, H<sub>3</sub>-12' and  $\delta_{\text{H}}$  1.78 (H<sub>a</sub>-1').

Two partial structures established by COSY (*vide supra*) remained to be incorporated in the growing scaffold. While H<sub>2</sub>-1' ( $\delta_{\text{H}}$  1.78, 2.12) and H<sub>2</sub>-2' ( $\delta_{\text{H}}$  1.76, 2.13) were heavily overlapped, an HMBC correlation between those shifts and  $\delta_{\text{C}}$  79.1 (C-2) extended the scaffold. The partial structure from COSY that included  $\delta_{\text{H}}$  5.11 (H-3') and 1.58 (H<sub>3</sub>-11') could be connected to C-2' based on an HMBC correlation between H-3' and C-2'. The final intervention of two methylene groups  $\delta_{\text{C}}$  39.6 (C-5') and 26.6 (C-6') and the terminal trisubstituted olefin was established by HMBC correlations between  $\delta_{\text{H}}$  1.99 (H-5') and  $\delta_{\text{C}}$  123.3 (C-3');  $\delta_{\text{H}}$  2.05 (H-6') and  $\delta_{\text{C}}$  135.8 (C-4') and 131.4 (C-8'); and  $\delta_{\text{H}}$  5.07 (H-7') and  $\delta_{\text{H}}$  17.7 (C-10'), completing the linear scaffold.

Two valences remained unfilled, and the molecular formula of the established scaffold was missing one oxygen. Establishing a pyran ring between C-9 and C-2 would satisfy these last structural features. The resultant chromene is unusual in its highly substituted aromatic ring, the position of carbon branches on the aromatic ring, and the level of oxidation on the aromatic ring.

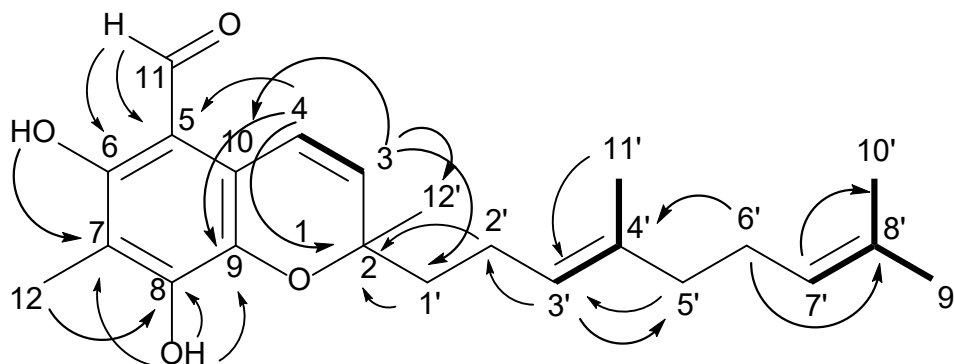


**Figure 2.** Proposed structure of tuaimenal A (**1**) based on NMR data. Key HMBC (→) and COSY (---) correlations are shown.

**Stereochemical Evaluation of Tuaimenal A (1).** Determination of the absolute configuration of tuaimenal A (**1**) was achieved using vibrational circular dichroism (VCD), a method which can be employed directly on chiral molecules in solution phase.<sup>19–22</sup> The monoterpene tail gave rise to a large number of low energy conformations, which presented a challenge for density-functional theory (DFT) calculations. A truncated version of the molecule was initially studied substituting an ethyl group for the monoterpene tail. This had a reduced number of low energy conformers (9) which were rapidly calculated for comparison to the experimental spectra. While there was some congruence, the overall comparison was not satisfactory. A thorough molecular mechanics search of tuaimenal A (**1**) yielded over 800 conformers in a 5 Kcal/mol range. Using a small Linux cluster with 64 available cores, DFT calculations were performed on all of the conformers at the B3LYP/6-31G(d) level.<sup>23</sup> After removing duplicates and higher energy structures, the resulting 338 unique conformers were

Boltzmann averaged to produce the final theoretical spectrum (**Fig. 3**). The *R* enantiomer was used for calculation, and a match to the measured spectrum confirmed the stereochemistry of tuaimenal A (**1**) as *R*. The comparison of experimental and theoretical spectra was quantified<sup>24,25</sup> using BioTools CompareVOA<sup>®</sup> software, with high neighborhood similarity for IR (90.6) and VCD (57.5), Enantiometric Similarity Index for VCD (35.6) and a confidence level of 86%. A fairly weak VCD signal gave rise to some noise in the experimental spectra which likely reduced the confidence level a bit. Visual comparison of the data makes clear that the assignment is correct, with 11 of the most intense VCD bands well correlated to the experimental data. Overall, this proved to be an effective method to determine the stereochemistry of tuaimenal A (**1**).

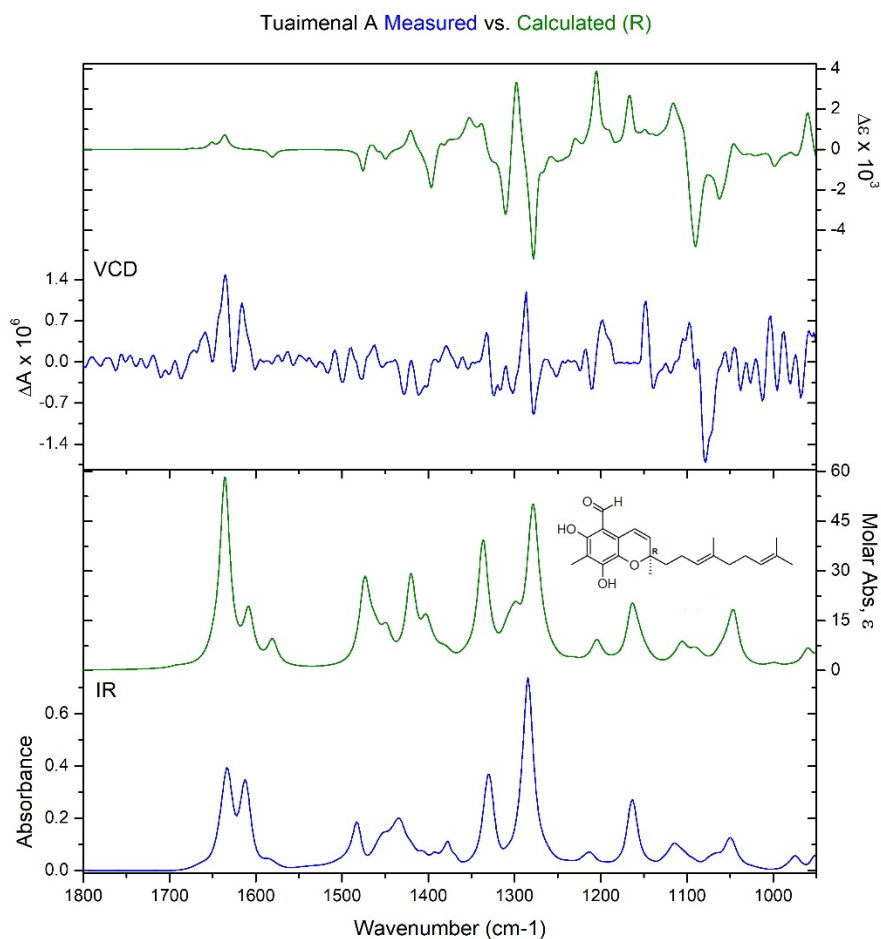


**Figure 3.** Stereochemistry at C-2 was determined to be the *R* configuration based on VCD analysis. Top graph shows the congruence between the calculated VCD for the *R* configured stereocenter (green) and the measured VCD (blue). In the lower graph, the calculated FTIR absorbance (green) also demonstrates congruence with the calculated data (blue).

**Rigid Docking of Tuaimenal A (1) in SARS-CoV-2 Protein Targets.** Schrodinger's Glide XP scoring function was utilized for ranking and analyzing tuaimenal A (**1**) poses. GlideScores are reported for each pose and represent a correlation between the protein-ligand complex and the binding free energy.<sup>26</sup> The criterion for selecting top poses was a threshold of -7.0 or lower, and ligands are considered to have favorable binding interactions with the target protein when presenting these scores. Validation of binding strength is observed when multiple ligand conformations are bound to multiple target conformations of the same protease.

Tuaimenal A (**1**) showed a promising profile for binding to both Mpro and PLpro (**Table 3**). Six optimal poses of tuaimenal A (**1**) were observed for three of the Mpro protease structures, of which the lowest GlideScore was -8.925, and an average score of -8.165. The favorable binding is attributed to both hydrogen bonding (yellow dotted lines) and pi-pi-stacking interactions (blue dotted lines) with (histidine) HSD 141, shown in (**Fig. 4**). Eleven hits resulted for three of the PLpro conformations (lowest -8.533, average 7.585). Seven poses successfully bound to three TMPRSS2 structures (lowest -8.282, average -7.750). One conformation of tuaimenal A (**1**) bound successfully to the protease structure for RdRp (-7.419). Low binding potentials are likely attributed to the fact that RdRP is generally inhibited through covalent interactions, rather than intermolecular.<sup>17</sup>

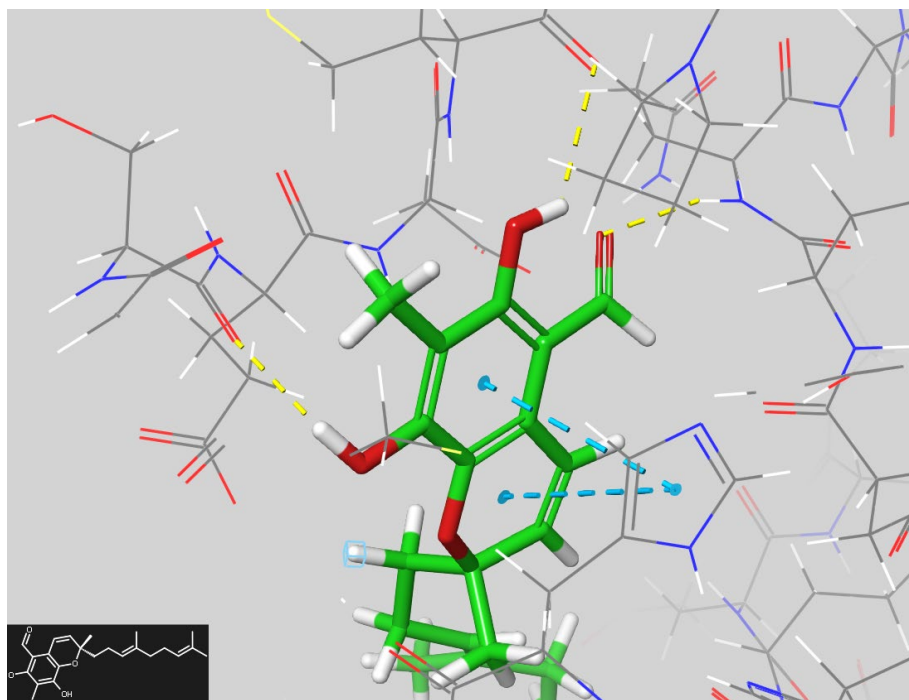


**Figure 4.** Final Pose of tuaimenal A (**1**) docking with Mpro structure 1, highlighting the two pi-pi stacking interactions with HSD 141, and three additional hydrogen bonds with GLN 189, MET 49, and SER 46.

**Table 3.** GlideScores for SARS-CoV-2 protein targets for the ligand conformations of tuaimenal A (**1**).

<i>Protease</i>	<i>GlideScores</i>
<i>mpro3</i>	-8.925
<i>mpro3</i>	-8.925
<i>mpro5</i>	-8.760
<i>plpro3</i>	-8.533
<i>plpro3</i>	-8.533
<i>tmpr4</i>	-8.282
<i>tmpr4</i>	-8.067
<i>tmpr4</i>	-7.896
<i>tmpr4</i>	-7.896
<i>plpro1</i>	-7.747
<i>plpro1</i>	-7.747
<i>tmpr1</i>	-7.721
<i>plpro1</i>	-7.600
<i>plpro1</i>	-7.600
<i>mpro1</i>	-7.577
<i>mpro1</i>	-7.577
<i>plpro1</i>	-7.465
<i>rdrp_ada</i>	-7.419
<i>tmpr3</i>	-7.295
<i>mpro1</i>	-7.250
<i>tmpr1</i>	-7.090
<i>plpro3</i>	-7.066
<i>plpro3</i>	-7.066
<i>plpro3</i>	-7.039
<i>plpro4</i>	-7.039

## CONCLUSIONS

The secondary metabolome of four specimens of Irish deep-sea coral, *Drifa* sp., was explored utilizing NMR-guided fractionation methods. The chemistry of the family Nephtheidae to which it belongs, has been previously described; however, this is the first analysis of the genus *Drifa*. A new natural product, tuaimenal A (**1**), was discovered. This meroterpene represents a

new carbon scaffold with a highly substituted chromene core and a monoterpene tail. The benzopyran ring system includes an aldehyde, two phenol features, and a methyl group. Tuaimenal A (**1**) demonstrates potential for inhibition of the main protease for SARS-CoV-2 based on *in silico* docking experiments. The discovery of this new natural product points to the importance of chemical explorations of deep-sea organisms. Careful sampling and analysis in cold water coral systems, including in Ireland's deep sea, can promote drug discovery efforts and underscore the importance of conservation of these natural resources.

## MATERIALS AND METHODS

**General Procedures.** Commercial silica gel 230-400 mesh was used to load samples for MPLC. MPLC was performed on a Teledyne Isco CombiFlash Rf200i with UV detection and a RediSep RF silica flash column. Semipreparative normal phase HPLC was performed on a Shimadzu LC-20 AT system with evaporative light scattering detector (ELSD) and UV detection using semipreparative (Phenomenex Luna Silica; 250 x 10 mm, 5  $\mu$ m) or analytical (Phenomenex Luna C18; 250 x 4.6 mm, 5  $\mu$ m) conditions. Semipreparative non-aqueous reverse phase was performed on a Shimadzu LC20-AT system with a photodiode array detector using semipreparative (Phenomenex Luna C18; 250 x 10 mm, 5  $\mu$ m) conditions. All solvents were HPLC grade (>99% purity) unless stated otherwise and were obtained from Fisher Scientific. All  $^1\text{H}$  NMR spectra were recorded at 298K on a Bruker Neo 400 MHz or on a Varian 500 MHz Direct Drive instrument with direct detection, and  $^{13}\text{C}$  NMR spectra were recorded at 100 or 125 MHz, respectively. Chemical shifts are reported with the residual chloroform ( $\delta_{\text{H}}$  7.27 ppm;  $\delta_{\text{C}}$  77.0 ppm) and methanol ( $\delta_{\text{H}}$  4.87, 3.31 ppm;  $\delta_{\text{C}}$  49.1 ppm) signals as internal standards for  $^1\text{H}$  and  $^{13}\text{C}$  spectra. IR spectrum was recorded with an Agilent Cary 630 FTIR spectrometer and a PerkinElmer Spectrum Two equipped with a UATR (single reflection diamond) sample

introduction system. UV absorptions were measured using an Agilent Cary 60 UV-Vis spectrophotometer. Optical rotation was measured using a Rudolph Research Analytical AUTOPOL IV digital polarimeter. HRESI MS experiments were obtained using an Agilent 6230 TOF LC-MS.

**Collection of *Drifa* sp. samples.** The four individuals of *Drifa* sp. were collected by *ROV Holland 1* from the deep sea (54.26007932 N, 11.58046619 W) at a depth of 823 meters during a 2018 cruise of *RV Celtic Explorer* (Cruise CE18012). *In situ* photographs were taken to aid in taxonomy and for collection metadata. Any epibionts were removed and a small voucher was removed and placed in 96% ethanol. The remainder of the biomass was frozen at -80 °C on board the *RV Celtic Explorer*. The samples were lyophilized upon arrival to National University of Ireland, Galway and stored at -20 °C, then transported to University of South Florida and stored at -20 °C until further processing.

**Extraction and Isolation of Natural Products.** Upon arrival at the University of South Florida, the specimens were extracted with 100% dichloromethane via reflux (40 °C) with a Soxhlet apparatus. From the 88 g of lyophilized sample, the 14.3 g of extract was obtained. A dichloromethane/water partition was performed, resulting in 13.7 g of extract in the organic layer. Initial separation was performed using NP MPLC with a silica column. A linear gradient of hexanes to ethyl acetate over thirty minutes, followed by isocratic 100% ethyl acetate for eight minutes, and then 20% methanol and 80% ethyl acetate for seven minutes. All resulting fractions were dried using passive air or nitrogen. Thirteen fractions were obtained and based on NMR spectroscopic data, the fourth through sixth fractions (eluting roughly around 0% to 35% ethyl acetate) were selected for further purification. Iterations of NP HPLC were performed leading to the isolation of 36.8 g of tuaimenal A (**1**).

Tuaimenal A (**1**): yellow oil;  $[\alpha]_{20D}$  0.7 (c 0.007, CHCl<sub>3</sub>); UV (ACN)  $\lambda_{\max}$  (log  $\epsilon$ ): 198 nm (3.2); IR  $\nu$  (thin film): 2980, 2930, 2880, 1633, 1612, 1483, 1329, 1284 cm<sup>-1</sup>; <sup>1</sup>H and <sup>13</sup>C NMR data, Table 1; HRESIMS  $m/z$  371.2216 [M + H]<sup>+</sup> (calculated for 371.2217, C<sub>23</sub>H<sub>31</sub>O<sub>4</sub>).

**Vibrational Circular Dichroism Measurements.** 5.7 mg of tuaimenal A (**1**) was dissolved in 220  $\mu$ L CDCl<sub>3</sub> and transferred to a BaF<sub>2</sub> IR cell with path length of 100  $\mu$ m. Instrumentation was a BioTools (Jupiter, Florida) ChiralIR 2X DualPEM FT-VCD, resolution 4 cm<sup>-1</sup>, PEM maximum frequency 1400 cm<sup>-1</sup>. The sample was measured for 24 blocks of 1 hour each while purged with dry air to remove water vapor. The IR was processed by solvent subtraction and offset to zero at 2000 cm<sup>-1</sup>. The VCD blocks were averaged, then subtracted using a solvent baseline to produce the final spectrum.

**Vibrational Circular Dichroism Calculations.** *R*-Tuaimenal A (**1**) was subjected to a GMMX (MMF94) search using BioTools ComputeVOA<sup>®</sup> software to find the lowest energy conformers in a 5 kcal/mol range. A total of 805 conformers were minimized using Gaussian 09 at the 631G(d)/B3LYP level with CPCM solvent (chloroform) model. IR and VCD frequencies were calculated at the same level, then duplicates were removed. The 338 lowest energy unique conformers were then Boltzmann averaged and plotted with a line width of 5 cm<sup>-1</sup>. IR and VCD spectra were then frequency scaled by a factor of 0.968 and compared to the experimental data.

**Ligand Preparation.** Tuaimenal A (**1**) was processed through the Maestro LigPrep function. Conformational states were created with a target pH of 7.0 +/- 2.0 using Epik. The structures were able to tautomerize and were desalted before final poses were given. The specified chirality of the molecule was retained. The generated ligands for tuaimenal A (**1**) were capped at 32 conformations of energetically minimized output structures.

**Protein Preparation and Grid Generation.** The Protein Data Bank (PDB) provided crystal structures for three of the four SARS-CoV2 targets; MPro (6LU7), RdRp (7BV2), and PLpro (6W9C). For the final protein, (TMPRSS2), the structure was created via a homology model using SWISS-MODEL. To mimic biological conditions for the molecular docking procedure, all four protein targets were solvated, neutralized, and equilibrated with the following process. First, all receptor targets were pre-processed through CHARMMing.org (CHARMM web interface and graphics) in order to determine ionization states (with PROPKA), add missing hydrogens, and assign correct bond orders. Each protein was then solvated with 46,656 TIP3 waters in a 90 x 90 x 90 Angstrom water box using CHARMM. The number of counterions needed to achieve a net zero charge for the system was calculated and randomly placed in the water box using a Monte Carlo based method. Next, the system was heated from 110K to 310K using CHARMM molecular dynamics over a 40 ns time scale. To ensure a low energy system, the system was then equilibrated with a 20 ns molecular dynamics simulation kept at 310K. From this equilibration MD trajectory, unique conformations of each protein target were selected through active-site RMSD clustering. Using an RMSD threshold of 2 Angstroms, an average of 7 unique protein conformations were generated for each SARS-CoV-2 protein target to be used in the docking procedure.

Final protein conformations generated from a flexible docking of antiviral compounds into these prepared protein systems were also used as targets for the rigid docking portion of this study. These final structures had adopted favorable conformations to accommodate large antiviral ligands through MD simulations as part of the flexible docking method.

Schrodinger's Protein Preparation Wizard program was used in the initial processing of the protein structures, bond orders were assigned, missing hydrogens were added, disulfide

bonds were created, waters beyond 5 Å from heterogroups were deleted, and het states were generated using Epik for a pH range of 7.0 +/- 2.0. After preprocessing was complete, water orientations were sampled and then optimized. Waters with less than 3 hydrogen bonds to non-hydrogen atoms were removed from the protein structure. The restrained minimization was performed in the final processing step, where heavy atoms were converged to an RMSD of 0.30 Å using an OPLS3e force field. The Glide Receptor Grid Generation function was applied to the prepared protein structures. For the optimized protease conformations, binding residues were specified, and the centroid of the selected residues served as the center of the binding site. Information on the residue numbers selected in the definition of the active site of each protein target can be found in Supporting Information (**Table S1**). After selecting the binding site, rotatable groups were visually selected based on proximity to the centroid and with careful consideration of any residue that would have obstructed the active site. Rotatable groups were selected separately for each conformation following these guidelines.

**Rigid Docking.** For the rigid docking portion of this study, Schrödinger's Glide application was utilized. Ligand sampling was set for flexible rotation to allow multiple spatial conformations to be sampled. The van der Waals radii of the ligand atoms was set to a scaling factor of 0.80 and a partial atomic charge cutoff of 0.15 to soften the potential when considering nonpolar regions of the ligands. As part of a screening program, the compound was first evaluated using high throughput virtual screening. SP (standard precision) docking was then performed, followed by XP (extra precision) docking.

## **ASSOCIATED CONTENT**

The following files are available free of charge.

The following Supporting Information is available:

<sup>1</sup>H, <sup>13</sup>C, 2D NMR, HRESIMS, UV, and FTIR spectra for tuaimenal A (1) (PDF)

Binding site residues for rigid docking with Mpro, Plpro, RdRp, and TMPRSS2 protein targets (PDF)

## **AUTHOR INFORMATION**

### **Corresponding Author**

\*Baker, Bill J., University of South Florida, Department of Chemistry, 4202 E. Fowler Ave. CHE205, Tampa, FL 33620; [bjbaker@usf.edu](mailto:bjbaker@usf.edu)

### **Author Contributions**

The manuscript was written through contributions of all authors. All authors have given approval to the final version of the manuscript.

This work was the result of a team effort in which the following contributions are recognized: methodology and experimentation, N.E.A., J.N., S.G.D., L.W., A.P., F.K., H.L.W, B.J.B; data analysis, N.E.A., J.N., S.G.D., L.W., A.P., F.K., R.M.Y, B.J.B; original draft preparation, N.E.A., B.J.B., J.N., S.G.D., L.W., A.P., F.K.,; review and editing, N.E.A., B.J.B., A.L.A., J.N., S.G.D., L.W., A.P., F.K., R.M.Y., M.P.J, H.L.W; funding acquisition, B.J.B. and A.L.A.

## **ACKNOWLEDGMENTS**

This publication has emanated from research supported by a research grant from Science Foundation Ireland (SFI) and the Marine Institute under the Investigators Programme Grant No. SFI/15/1A/3100, co-funded under the European Regional Development Fund 2014-2020 to

A.L.A., and also the project NMBLI (Grant-Aid Agreement PBA/MB/16/01). Research at USF was supported NIH Grant R56 AI154922 (to B.J.B. and Dr. L.N. Shaw). Subsea photographs taken by NUI Galway, copyright Marine Institute, during cruise CE18012 funded under SFI/15/1A/3100. S. Afoullouss is acknowledged for his assistance with sample collection and initial processing. We gratefully acknowledge the assistance of the science party and crew of the *RV Celtic Explorer* and the pilots of the *ROV Holland I*, without whose distinctive expertise this research would not be possible. The students G. Shaw, S. Suarez, and M. Silas are recognized for their technical assistance with this project. We also recognize the assistance of Dr L. Calcul and J. Welsch with the Chemical Purification, Analysis, and Screening Facility at USF.

## REFERENCES

- (1) Roberts, J. M.; Wheeler, A.; Freiwald, A.; Cairns, S. *Cold-Water Corals: The Biology and Geology of Deep-Sea Coral Habitats*; Cambridge University Press, 2009.
- (2) Skropeta, D.; Wei, L. Recent Advances in Deep-Sea Natural Products. *Nat. Prod. Rep.* **2014**, *31* (8), 999–1025. <https://doi.org/10.1039/c3np70118b>.
- (3) Skropeta, D. Deep-Sea Natural Products. *Nat. Prod. Rep.* **2008**, *25* (6), 1131. <https://doi.org/10.1039/b808743a>.
- (4) Blunt, J.; Copp, B. R.; Keyzers, R. A.; Herbert, M.; Munro, G. Marine Natural Products Natural Product Reports. *Nat. Prod. Rep.* **2016**, *33* (March), 382–431. <https://doi.org/10.1039/C5NP00156K>.
- (5) Daly, M.; Brugler, M. R.; Cartwright, P.; Collins, A. G.; Dawson, M. N.; Fautin, D. G.; France, S. C.; Mcfadden, C. S.; Opresko, D. M.; Rodriguez, E. The Phylum Cnidaria: A Review of Phylogenetic Patterns and Diversity 300 Years after Linnaeus. **2007**.
- (6) Harper, M. K.; Bugni, T. S.; Copp, B. R.; James, R. D.; Lindsay, B. S.; Richardson, A. D.;

- Schnabel, P. C.; Tasdemir, D.; VanWagoner, R. M.; Verbitski, S. M. Marine Chemical Ecology. *McClintock, JB Bak. BJ eds.; Boca Raton, Florida* **2001**.
- (7) Hu, J.; Yang, B.; Lin, X.; Zhou, X.; Yang, X.; Long, L.; Liu, Y. Chemical and Biological Studies of Soft Corals of the Nephtheidae Family. *Chem. Biodivers.* **2011**, *8* (6), 1011–1032. <https://doi.org/10.1002/cbdv.201000105>.
- (8) Wang, H.; Li, X.; Li, T.; Zhang, S.; Wang, L.; Wu, X.; Liu, J. The Genetic Sequence, Origin, and Diagnosis of SARS-CoV-2. *Eur. J. Clin. Microbiol. Infect. Dis.* **2020**, *39* (9), 1629–1635. <https://doi.org/10.1007/s10096-020-03899-4>.
- (9) Luan, B.; Huynh, T.; Cheng, X.; Lan, G.; Wang, H. R. Targeting Proteases for Treating COVID-19. *J. Proteome Res.* **2020**, *19* (11), 4316–4326. <https://doi.org/10.1021/acs.jproteome.0c00430>.
- (10) Zhai, P.; Ding, Y.; Wu, X.; Long, J.; Zhong, Y.; Li, Y. The Epidemiology, Diagnosis and Treatment of COVID-19. *Int. J. Antimicrob. Agents* **2020**, *55* (5). <https://doi.org/10.1016/j.ijantimicag.2020.105955>.
- (11) Dong, E.; Du, H.; Gardner, L. An Interactive Web-Based Dashboard to Track COVID-19 in Real Time. *Lancet Infect. Dis.* **2020**, *20* (5), 533–534. [https://doi.org/10.1016/S1473-3099\(20\)30120-1](https://doi.org/10.1016/S1473-3099(20)30120-1).
- (12) Beigel, J. H.; Tomashek, K. M.; Dodd, L. E.; Mehta, A. K.; Zingman, B. S.; Kalil, A. C.; Hohmann, E.; Chu, H. Y.; Luetkemeyer, A.; Kline, S.; Lopez de Castilla, D.; Finberg, R. W.; Dierberg, K.; Tapson, V.; Hsieh, L.; Patterson, T. F.; Paredes, R.; Sweeney, D. A.; Short, W. R.; Touloumi, G.; Lye, D. C.; Ohmagari, N.; Oh, M.; Ruiz-Palacios, G. M.; Benfield, T.; Fätkenheuer, G.; Kortepeter, M. G.; Atmar, R. L.; Creech, C. B.; Lundgren, J.; Babiker, A. G.; Pett, S.; Neaton, J. D.; Burgess, T. H.; Bonnett, T.; Green, M.;

- Makowski, M.; Osinusi, A.; Nayak, S.; Lane, H. C. Remdesivir for the Treatment of Covid-19 — Final Report. *N. Engl. J. Med.* **2020**, *383* (19), 1813–1826. <https://doi.org/10.1056/nejmoa2007764>.
- (13) Fehr, A. R.; Perlman, S. Coronaviruses: An Overview of Their Replication and Pathogenesis. In *Coronaviruses: Methods and Protocols*; 2015; Vol. 1282, pp 1–23. [https://doi.org/10.1007/978-1-4939-2438-7\\_1](https://doi.org/10.1007/978-1-4939-2438-7_1).
- (14) Anand, K.; Ziebuhr, J.; Wadhwani, P.; Mesters, J. R.; Hilgenfeld, R. ( 3CL pro ) Structure : Basis for Design of Anti-SARS Drugs. *Science (80-. )*. **2003**, *300* (June), 1763–1767.
- (15) Zhang, L.; Lin, D.; Sun, X.; Curth, U.; Drosten, C.; Sauerhering, L.; Becker, S.; Rox, K.; Hilgenfeld, R. Crystal Structure of SARS-CoV-2 Main Protease Provides a Basis for Design of Improved  $\alpha$ -Ketoamide Inhibitors. *Science (80-. )*. **2020**, *368* (6489), 409–412. <https://doi.org/10.1126/science.abb3405>.
- (16) Hoffmann, M.; Kleine-Weber, H.; Schroeder, S.; Krüger, N.; Herrler, T.; Erichsen, S.; Schiergens, T. S.; Herrler, G.; Wu, N. H.; Nitsche, A.; Müller, M. A.; Drosten, C.; Pöhlmann, S. SARS-CoV-2 Cell Entry Depends on ACE2 and TMPRSS2 and Is Blocked by a Clinically Proven Protease Inhibitor. *Cell* **2020**, *181* (2), 271–280.e8. <https://doi.org/10.1016/j.cell.2020.02.052>.
- (17) Yin, W.; Luan, X.; Li, Z.; Zhou, Z.; Wang, Q.; Gao, M.; Wang, X.; Zhou, F.; Shi, J.; You, E.; Liu, M.; Wang, Q.; Jiang, Y.; Jiang, H.; Xiao, G.; Zhang, L.; Yu, X.; Zhang, S.; Eric Xu, H. Structural Basis for Inhibition of the SARS-CoV-2 RNA Polymerase by Suramin. *Nat. Struct. Mol. Biol.* **2021**, *28* (3), 319–325. <https://doi.org/10.1038/s41594-021-00570-0>.

- (18) Tauimenal (pronounced twam-en-al) is derived from tuaimneacha, the Irish Gaelic word used to describe the sound of waves crashing against the rocks.
- (19) He, Y.; Bo, W.; Dukor, R. K.; Nafie, L. A. Determination of Absolute Configuration of Chiral Molecules Using Vibrational Optical Activity: A Review. *Appl. Spectrosc.* **2011**, *65* (7), 699–723. <https://doi.org/10.1366/11-06321>.
- (20) Merten, C.; Golub, T. P.; Kreienborg, N. M. Absolute Configurations of Synthetic Molecular Scaffolds from Vibrational CD Spectroscopy. *J. Org. Chem.* **2019**, *84* (14), 8797–8814. <https://doi.org/10.1021/acs.joc.9b00466>.
- (21) Polavarapu, P. L.; Santoro, E. Vibrational Optical Activity for Structural Characterization of Natural Products. *Nat. Prod. Rep.* **2020**, *37* (12), 1661–1699. <https://doi.org/10.1039/D0NP00025F>.
- (22) Chamberlain, B. T.; Vincent, M.; Na, J.; Mu, P.; Greka, A.; Wagner, F. F. Multigram Preparation of BRD4780 Enantiomers and Assignment of Absolute Stereochemistry. **2020**. <https://doi.org/10.1021/acs.joc.0c02520>.
- (23) Devlin, F. J.; Stephens, P. J.; Cheeseman, J. R.; Frisch, M. J. Ab Initio Prediction of Vibrational Absorption and Circular Dichroism Spectra of Chiral Natural Products Using Density Functional Theory:  $\alpha$ -Pinene. *J. Phys. Chem. A* **1997**, *101* (51), 9912–9924. <https://doi.org/10.1021/jp971905a>.
- (24) Polavarapu, P. L.; Covington, C. L. Comparison of Experimental and Calculated Chiroptical Spectra for Chiral Molecular Structure Determination. *Chirality* **2014**, *26* (9), 539–552. <https://doi.org/10.1002/chir.22316>.
- (25) Debie, E.; De Gussem, E.; Dukor, R. K.; Herrebout, W.; Nafie, L. A.; Bultinck, P. A Confidence Level Algorithm for the Determination of Absolute Configuration Using

Vibrational Circular Dichroism or Raman Optical Activity. *ChemPhysChem* **2011**, *12* (8), 1542–1549. <https://doi.org/10.1002/cphc.201100050>.

- (26) Friesner, R. A.; Murphy, R. B.; Repasky, M. P.; Frye, L. L.; Greenwood, J. R.; Halgren, T. A.; Sanschagrin, P. C.; Mainz, D. T. Extra Precision Glide: Docking and Scoring Incorporating a Model of Hydrophobic Enclosure for Protein-Ligand Complexes. *J. Med. Chem.* **2006**, *49* (21), 6177–6196. <https://doi.org/10.1021/jm051256o>.